The Meteoritical Society

Meteoritics & Planetary Science 1–18 (2013)
doi: 10.1111/maps.12172

Opaque minerals, magnetic properties, and paleomagnetism of the Tissint Martian meteorite

Jérôme GATTACCECA[1,2*], Roger H. HEWINS[3], Jean-Pierre LORAND[4], Pierre ROCHETTE[1], France LAGROIX[5], Cécile COURNÈDE[1], Minoru UEHARA[1], Sylvain PONT[3], Violaine SAUTTER[3], Rosa. B. SCORZELLI[6], Chrystel HOMBOURGER[7], Pablo MUNAYCO[6], Brigitte ZANDA[3,8], Hasnaa CHENNAOUI[9], and Ludovic FERRIÈRE[10]

[1]CNRS, Aix-Marseille Université, CEREGE UM34, Aix-en-Provence, France
[2]Department of Earth, Atmospheric, and Planetary Sciences, Massachusetts Institute of Technology, Cambridge, Massachusetts 02139, USA
[3]Laboratoire de Minéralogie et Cosmochimie du Muséum, MNHN, UMR 7202 Paris, France
[4]Laboratoire de planétologie et géodynamique de Nantes, UMR 6112, Université de Nantes, Faculté des Sciences, Nantes, France
[5]Institut de Physique du Globe de Paris, Paris, France
[6]Centro Brasileiro de Pesquisas Físicas, Rio de Janeiro, Brazil
[7]CAMECA SAS, Gennevilliers, France
[8]Department of Earth and Planetary Sciences, Rutgers University, Piscataway, New Jersey 08854, USA
[9]Department of Geochemistry of Earth Sciences, Hassan II University, Casablanca, Morocco
[10]Natural History Museum, Vienna, Austria
[*]Corresponding author. E-mail: gattacceca@cerege.fr

(Received 19 December 2012; revision accepted 24 June 2013)

Abstract–We present a description of opaque minerals, opaque mineral compositions, magnetic properties, and paleomagnetic record of the Tissint heavily shocked olivine-phyric shergottite that fell to Earth in 2011. The magnetic mineralogy of Tissint consists of about 0.6 wt% of pyrrhotite and 0.1 wt% of low-Ti titanomagnetite (in the range ulvöspinel 3–15 magnetite 85–97). The titanomagnetite formed on Mars by oxidation-exsolution of ulvöspinel grains during deuteric alteration. Pyrrhotite is unusual, with respect to other shergottites, for its higher Ni content and lower Fe content. Iron deficiency is attributed by an input of regolith-derived sulfur. This pyrrhotite has probably preserved a metastable hexagonal monosulfide solution structure blocked at temperature above 300 °C. The paleomagnetic data indicate that Tissint was magnetized following the major impact suffered by this rock while cooling at the surface of Mars from a post-impact equilibrium temperature of approximately 310 °C in a stable magnetic field of about 2 μT of crustal origin. Tissint is too weakly magnetic to account for the observed magnetic anomalies at the Martian surface.

INTRODUCTION

The discovery of the intense crustal magnetic anomalies on Mars was a major result of recent Martian exploration (Acuña et al. 1999; Langlais et al. 2010). However, although there is little doubt that a core dynamo was necessary to magnetize the crust, the lithology of the source of the large crustal remanent magnetization observed today remains puzzling (e.g., Quesnel et al. 2009). Martian meteorites are the only samples from Mars available to date. Although they provide a biased sampling of the Martian crust, the study of their magnetic properties may provide clues to the understanding of Martian crustal magnetism, and hence crustal magnetic mineralogy and dynamics.

Opaque minerals in Martian meteorites have been, in general, studied for information on the evolution of Martian magmas and their oxidation state (e.g., Goodrich et al. 2003; Lorand et al. 2005). On the other hand, the magnetic properties (e.g., Rochette et al.

© The Meteoritical Society, 2013.

2005) and paleomagnetism (e.g., Cisowski 1986) of nakhlites and shergottites provide the following general picture: these meteorites contain pyrrhotite and/or (titano)magnetite as magnetic minerals, and they most likely record Martian surface fields of crustal remanent origin (Cisowski 1986; Gattacceca and Rochette 2004). However, these studies usually originate from different disciplinary groups (petrologists and mineralogists on one hand, rock magnetists and paleomagnetists on the other hand) and have never been really integrated.

In this work, we combine the study of opaque minerals, as well as magnetic properties and the paleomagnetic record of the Tissint olivine-phyric shergottite, to identify which phases carry the magnetization and how this magnetization was acquired. This is the first detailed study envisioning the balance of all potential magnetic carriers (i.e., Fe-Ti oxides, chromites, and Fe-Ni sulfides) in an olivine-phyric shergottite.

The Tissint meteorite, which fell in July 2011 in Morocco, is an olivine-phyric shergottite (as defined by Goodrich 2002), and only the fifth recovered Martian meteorite fall (Chennaoui Aoudjehane et al. 2012). It offers the opportunity to study the magnetic mineralogy and the paleomagnetic signal of a sample from Mars that has not suffered terrestrial weathering. This pristine character is crucial for two main reasons: the absence of terrestrial weathering minerals, some of which are ferromagnetic (notably those replacing Fe-Ni sulfides; Lorand et al. 2005), and also the better preservation of the paleomagnetic signal of such a meteorite fall.

MATERIALS AND METHODS

We have been able to work on 35 samples from the Tissint meteorite, with mass ranging from 30 mg to 29 g. The first samples were available in our laboratory only 6 months after the fall. We have measured the following magnetic properties: natural and artificial remanences and their behavior upon thermal pressure and alternating field (AF) demagnetization, hysteresis parameters at room and low temperatures, anisotropy of magnetic susceptibility. We also used magneto-optical imaging coupled with high spatial resolution electron microprobe analyses, and Mössbauer spectroscopy. In view of the large numbers of acronyms and the nonintuitive units used in used rock magnetism, we provide an overview of the magnetic properties discussed in this work in Table S1.

Low-temperature (LT) hysteresis measurements were performed with a Princeton® Micromag Vibrating Sample Magnetometer equipped with a LT cryostat and a maximum applied field of 1 T. High-temperature hysteresis measurements were also performed on a Princeton VSM equipped with a high-temperature furnace and a maximum applied field of 1.8 *T*. Moment sensitivity of the VSM is approximately 5×10^{-9} Am^2. The analysis of hysteresis loops provided the ratio of saturation remanent magnetization (M_{RS}) to saturation magnetization (M_S) and the coercive force (B_C). High-field susceptibility (χ_{HF}) was determined by a linear fit for applied fields >0.9 T of the hysteresis loops. Remanent coercive force (B_{CR}) was determined by DC back-field experiments performed with the VSM. Other low-temperature measurements were performed with an MPMS from Quantum Design®. This instrument has a moment sensitivity of 10^{-11} Am^2, and can operate in the 1.9–400 K temperature range.

The low-field specific susceptibility (written as χ in m^3 kg^{-1}) and its anisotropy were measured using Agico MFK1 apparatus with sensitivity of 5×10^{-13} m^3, operating at 200 A m^{-1} peak field and a frequency of 976 Hz. The anisotropy of magnetic susceptibility was characterized by the shape parameter T (Jelinek 1981), and the anisotropy degree P (ratio of maximum to minimum susceptibility). The anisotropy of isothermal remanent magnetization (IRM) was measured using a three-position scheme, and was characterized in the same way by P_{IRM} and T_{IRM}.

All remanence measurements were performed with a SQUID cryogenic magnetometer (2G Enterprises, model 755R, with noise level of 10^{-11} Am^2) with an attached automatic AF 3-axis degausser system (maximum peak field 170 mT) placed in a magnetically shielded room. To avoid the possible acquisition of gyroremanent magnetization during AF demagnetization, we used the Zijderveld-Dunlop correction method (Stephenson 1993) above 40 mT AF. Thermal demagnetization and acquisition of partial or total thermoremanent magnetizations were performed using an MMTD furnace, under argon atmosphere above 250 °C. IRM were imparted using a pulse magnetizer from Magnetic Measurements. IRM acquisition curves were obtained using the VSM. Remagnetization under pressure (PRM: piezoremanent magnetization, an analog for the magnetization acquired by rocks during a shock event in the presence of an ambient field) was studied using a nonmagnetic pressure cell and experimental settings described in Gattacceca et al. (2010a). To determine the nature of the natural remanent magnetization (NRM), we compare its coercivity (AF levels at which it is demagnetized) and unblocking temperature (temperature at which is it demagnetized) spectra with different artificial remanences: SIRM (saturation IRM), TRM (thermoremanent magnetization), and pTRM (partial thermoremanent magnetization).

All magnetic measurements were performed at CEREGE (Aix-en-Provence, France), with the exception of Mössbauer spectroscopy (at CBPF, Rio de Janeiro,

Table 1. Selected analyses of pyrrhotite.

	Incl in olivine			Matrix magmatic sulfides			Shock droplets			Del Norte County troilite		
										$n = 5$	$n = 36$[a]	$n = 10$[b]
Fe	54.1	54.1	56.0	56.5	57.9	57.85	59.1	61.9	61.8	63.45 (0.05)	63.43 (0.23)	63.30 (0.30)
Ni	6.9	6.2	4.8	4.8	4.5	3.0	1.4	1.2	1.27			
S	38.9	39.5	39.1	37.6	38.57	38.75	39.5	36.7	36.6	36.53 (0.03)	36.56 (0.20)	36.31 (0.20)
	SEM	EMPA	SEM	SEM	SEM	EMPA	SEM	SEM	EMPA	SEM	EMPA	EMPA
M/S	0.88	0.875	0.89	0.95	0.91	0.89	0.88	0.99	0.99	0.999	0.998	1.000

Results are in wt%. M/S, metal/sulfur (atomic ratio). Del Norte County is a terrestrial troilite used as external standard. SEM, scanning electron microscope standardless procedure (MNHN); EMPA, electron microprobe analyses (Camparis).
[a]Chevrier et al. (2011).
[b]Lorand et al. (2012).

Brazil), MPMS (at IPGP, Paris, France), and high-temperature VSM measurements (at IRM, Minneapolis, MN, USA).

Magneto-optical observations were performed using a system modified from that described by Uehara et al. (2010). In the previous method, the Faraday rotation angle, that is a calibrated function of the surface magnetic field, was computed from the brightness of the magneto-optical image. However, the accuracy of this method strongly depends on the brightness of the light source and the unevenness of the lightning within the field of view. A new optical microscope system with a fixed polarizer and a motor-controlled rotatable analyzer has been developed to measure the Faraday rotation angle directly. This system takes several images at different polarizer-analyzer angles (θ) by rotating the analyzer. At small angles (less than ±5°), the brightness of a given pixel (I) can be approximated by a parabolic function of θ, given by $I(\theta) = a\theta^2 + q$, where a and q are positive constants linked to the illumination and the quality of the polarizers. The brightness is minimum when the analyzer and the polarizer are crossed (θ = 0). When a magneto-optically active film (hereafter called "indicator") is mounted on the magnetized polished sample, the polarization plane is rotated in the indicator by a Faraday rotation angle α_F that is a function of the magnetic field intensity. As a result, the above equation becomes $I(\theta) = a(\theta - \alpha_F)^2 + q$. Thus, α_F, that is independent from the illumination (a and q), can be determined precisely by polynomial fitting of $I(\theta)$, and a map of α_F (and therefore of the magnetic field) can be obtained by conducting such fitting over the entire image (1024 × 1024 pixels). The entire procedure, including image stacking to reduce the signal–noise ratio, is controlled by LabVIEW software.

The ^{57}Fe Mössbauer spectroscopy was performed in transmission geometry at room temperature. Measurements were performed at high velocity (12 mm s^{-1}), using a 90 mg cm^{-2} absorber of the bulk meteorite sample with recording time of 1 month. Normos code (Brand 1995) was used for the spectral analysis.

Wavelength-dispersive quantitative analyses of oxide minerals were made on the Cameca SXFive electron microprobe at the Camparis EMP center (Université Paris VI), using 15 keV and 10 nA, and on the SXFiveFE probe at Cameca SAS (Gennevilliers), using 10 keV and 10 nA. The oxides were imaged on a Tescan VEGA II LSU SEM in conventional mode, and characterized with an SD3 (Bruker) EDS detector at the LMCM in the Muséum National d'Histoire Naturelle, Paris (France). Sulfides were analyzed by WDS at the Camparis EMP center (a few grains analyzed in one polished section) and by an EDS standardless procedure (Tescan VEGA II LSU SEM, Muséum National d'Histoire Naturelle, Paris) after careful imaging of each grain in the BSE mode to avoid phase-mixing contaminations. SEM was preferred over EMP for its better spatial resolution (a few hundred nanometers versus a few square micrometers), allowing fine pentlandite-pyrrhotite intergrowths to be resolved. The accuracy and precision of SEM analyses were checked by replicate analyses of a terrestrial troilite (Del Norte County, California; Chevrier et al. 2011; Lorand et al. 2012). Both analytical procedures agree within analytical uncertainties (Table 1).

OPAQUE MINERAL PETROGRAPHY AND COMPOSITION

The olivine-phyric shergottites (Goodrich 2002), in general, contain pyrrhotite and the following oxides: chromite, ulvöspinel, ilmenite (Herd et al. 2002; Goodrich et al. 2003; Gross et al. 2011). Petrographic observations of Tissint showed the presence of chromite, ilmenite, ulvöspinel (these oxides amounting to less than 1 wt% in total), and pyrrhotite (Chennaoui Aoudjehane et al. 2012). Among these minerals, pyrrhotite (Rochette et al. 2001) and chromite (Yu et al. 2001) can be ferromagnetic at room temperature, depending on their composition. It has also been proposed that peculiar Fe-Cr-Ti spinels may account for the magnetic properties of some shergottites (Yu and

Gee 2005). We present here detailed petrographic observations and chemical analysis of sulfides and oxides. A list of opaque minerals discussed in this work is provided in Table S2.

Mineralogy of Fe-Ni Sulfides

Tissint sulfides show some particularities compared with shergottites and other SNC meteorites investigated so far for sulfide mineralogy. Two distinct populations of sulfide grains are observed, one predating the major shock suffered by Tissint, and a second one formed during this shock event (Fig. S1). The first population consists of polyhedral grains, regularly shaped to anhedral grains between a few micrometers up to several tens of micrometers in size, as encountered in the other olivine-phyric shergottites (Goodrich 2002). These grains are all located at multiple junctions of major silicates (pyroxene, maskelynite, less commonly neighboring chromite; Fig. 1D). Such grains have been reported in all SNC meteorites studied so far for sulfide minerals, regardless of shock intensities (Lorand et al. 2005, 2012; Chevrier et al. 2011). They are considered crystallization products from magmatic sulfide melts trapped in the rock porosity during the igneous crystallization history. They will be referred to as "magmatic" sulfides in the following. We include in this group the rare sulfide grains found in magmatic inclusions of olivine megacrysts (Figs. 1B and 1C). Some magmatic sulfides are partially remelted (Fig. 1E) or seem to contain bubbles (Figs. 1F and 1G). We interpret this as textural evidence that some shock-related sulfides partly derive from erosion of pre-existing magmatic sulfides that first become cloudy and spongy (e.g., Walton and Spray 2003). The shock-related droplet-shaped blebs are smaller (10 μm on average), and are organized as network-forming cells inside remelted areas of the rock, which we interpret as recondensation of vaporized sulfide that was separated from glassy material (e.g., Sutton et al. 2008). Shock pyrrhotite droplets in glassy areas define a S-loss trend toward troilite composition, irrespective of Ni content. This trend is interpreted as partial devolatilization of S, as recently documented in great detail in NWA 2737, a highly shocked chassignite (Lorand et al. 2012).

Some pyrrhotite analyses are given by Chennaoui Aoudjehane et al. (2012), and we present here new analyses on about 80 individual sulfide grains from 36 locations throughout two polished sections (Table 1). Compared with all pyrrhotite analyzed so far in shergottites and nakhlites, Tissint pyrrhotites are poor in metal, i.e., they have a lower (Fe+Ni)/S ratio, regardless of the Fe/Ni ratio. Metal/sulfur ratio of magmatic grains shows considerable scatter between monoclinic-type (Fe_7S_8) and hexagonal-type (Fe_9S_{10}) endmembers (Fig. 2). This scatter is reproduced in both analytical procedures (EMP WDS and SEM EDS), although the SEM analyses tend to cluster around the monoclinic-type composition. However, there is no reason to assume analytical bias as: (1) the SEM analyses of Del Norte County troilite perfectly match the composition of stoichiometric troilite (FeS) and (2) both EMP and SEM procedures produce similar variation in the M/S ratios (from 0.86 to 0.92 for magmatic grains and 0.87–1.03 for shock droplets). The scatter in Fig. 2 is probably reflecting actual compositional variations (note the much higher number of SEM analyses compared with EMP analyses) rather than analytical bias generated by either of the two analytical methods.

Ni contents are highly homogeneous on the scale of individual grains (relative standard deviation better than 10%), but vary according to location of sulfides (Fig. 2). The most Ni-rich pyrrhotites are hosted in inclusions in olivine. Magmatic pyrrhotite grains associated with pyroxene clusters are poorer in Ni (4–5 wt% Ni). Shock pyrrhotite droplets show uniformly depleted Ni contents around 1–2 wt%. This Ni variation pattern cannot be ascribed to contamination of spot analyses by micron-sized pentlandite. Pentlandite is very scarce in Tissint pyrrhotite compared with similar olivine-phyric shergottites. Pentlandite only occurs as a few tiny flame-shaped blebs always concentrated on discontinuities such as fracture planes or grain edges, leaving large pyrrhotite cores free from pentlandite (Figs. 1B and 1C). If the pyrrhotite analyses were polluted by such pentlandite flames, then the Ni content should positively correlate with metal/sulfur, as documented in the shergottites previously studied for sulfide mineralogy (Lorand et al. 2005). Clearly, this is not the case (Fig. 2).

Tissint pyrrhotite shows metal/sulfur values displaced toward the monoclinic-type endmember with a tail of values plotting inside the two-phase field hexagonal (Hpo) + monoclinic (Mpo) pyrrhotite and intermediate pyrrhotite hexagonal structures (Fe_9S_{10} to FeS). This is, at first glance, inconsistent with whole-rock magnetic measurements (see below) that seem to rule out low-T ordered monoclinic pyrrhotite structure as the major magnetic carrier. To reconcile observations and magnetic measurements, we have to consider the following alternatives: (1) two-phase pyrrhotite intergrowth and (2) high-temperature, metastable disordered hexagonal pyrrhotite solid solution (monosulfide solid solution; Mss) showing more flexibility in metal/sulfur ratios. No intergrowths have been detected in the BSE mode; hence, the first interpretation lacks evidence. By contrast, the second

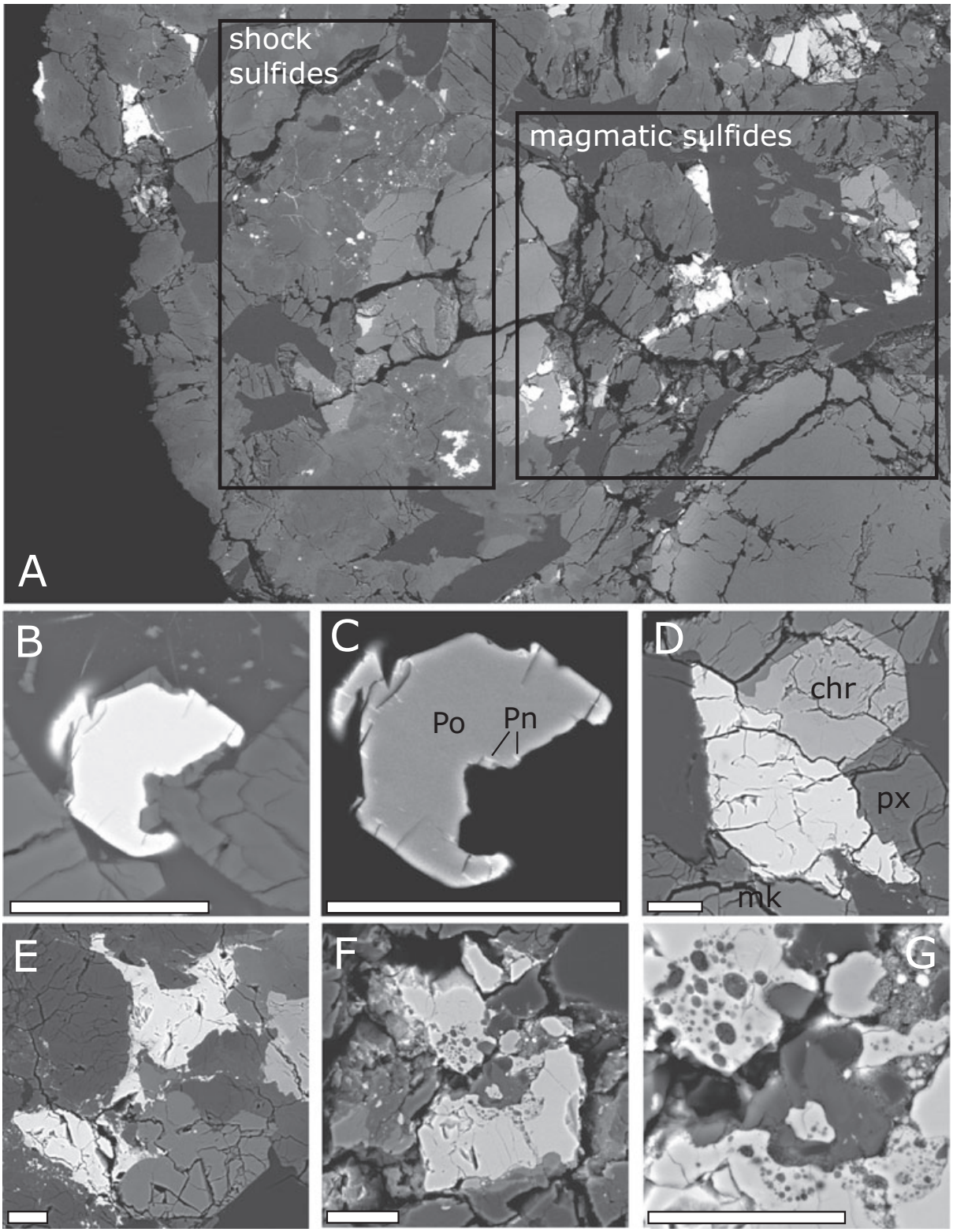

Fig. 1. Backscattered electron images of Tissint sulfides. Scale bar is 20 μm except for A. A) Illustration of the two sulfide textures described in the text. Field of view = 2 mm. B,C) pyrrhotite inclusion inside magmatic inclusion of olivine megacryst. Enhanced contrast in C reveals small pentlandite grains (Po, pyrrhotite; Pn, pentlandite). D) Unmodified magmatic pyrrhotite (mk, maskelynite; chr, chromite; px, pyroxene). E) Partly remelted magmatic sulfide. F) Magmatic sulfide with bubbling zone inside the pyrrhotite. G) Detail of F.

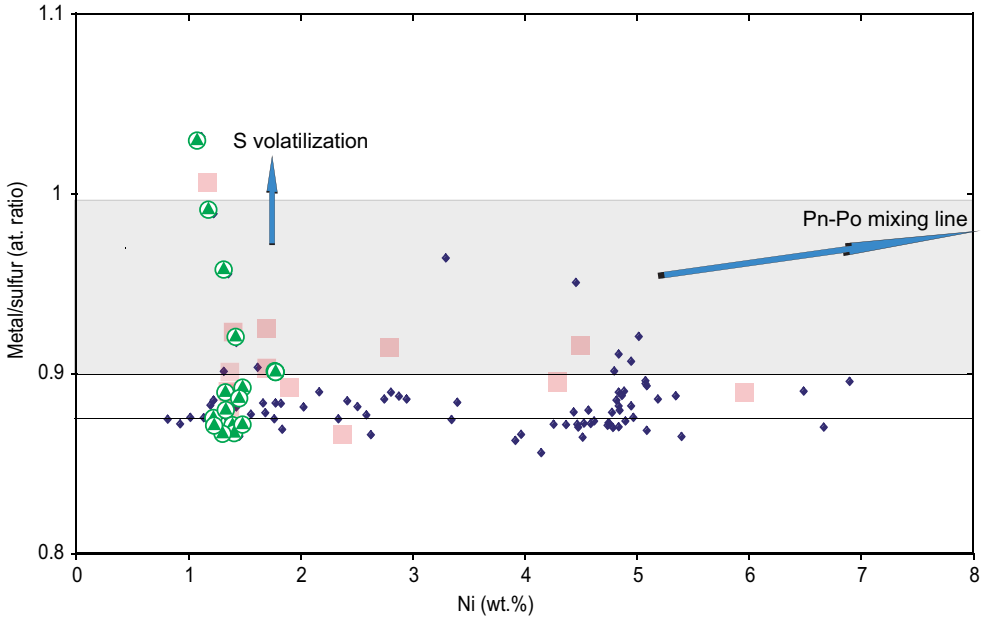

Fig. 2. Compositional features of Tissint Fe-Ni sulfides. Diamonds and triangle: standardless scanning electron microscope energy dispersive analyses calibrated with Del Norte County troilite (triangles: shock melted sulfides); squares: wavelength-dispersive electron microprobe analyses (Camparis). Shaded area: Shergottite pyrrhotite compositional range (free from terrestrial weathering; Lorand et al. 2005). The pentlandite-pyrrhotite (Pn-Po) mixing arrow assumes hexagonal-type (Fe_9S_{10}) pyrrhotite endmember contaminated by pentlandite (Fe/Ni at. = 1).

alternative is supported by the high Ni contents that are clearly in solid solution inside the pyrrhotite lattice. Mss is characterized by complete miscibility between Fe and Ni and metal/sulfur ratios covering the whole range of metal/sulfur ratio of natural pyrrhotite, while possessing a 1C, disordered hexagonal structure (Fleet [2006] and references therein). Tissint pyrrhotite compositions actually plot inside the Mss field at T = 400 °C, while a few analyses protrude into the S-rich side of the Mss stability field at 300 °C in the Fe-Ni-S ternary diagrams (Fig. S1). This indicates that Ni diffusion and structural rearrangement were blocked within the temperature range 300–400 °C. Cooling below 300° should convert the Ni into pentlandite while unmixing Hpo and Mpo. Incipient pentlandite exsolution occurring only on defects, fracture planes, and outer rims indicates heterogeneous nucleation processes that are thought to occur well above 250 °C in Mss. However, the kinetics of re-equilibration strongly depend on pyrrhotite composition. For instance, metal-poor (vacancy-rich) compositions inhibit the exsolution of pentlandite (Etaschmann et al. 2004). To summarize, Tissint pyrrhotites probably have preserved a metastable Mss structure blocked at temperatures above 300 °C. The contrasting Ni partitioning between olivine hosted grains and matrix pyrrhotites reflects the larger amount of Ni available for Ni-Fe exchange inside olivine. Conversely, the Ni-poor composition of shock sulfides is related to the Ni-poor compositions of shock melts and/or quick reheating/cooling after the shock peak.

However, our interpretation leaves open other issues such as the influence of several percent Ni on pyrrhotite magnetic properties or the contributions of both populations of sulfides (magmatic, shock-derived) to bulk magnetic properties (it is worth pointing out that some shock sulfides are close to single-domain grains in terms of grain size). The question that also arises is why Tissint magmatic pyrrhotite is so metal-deficient. Only the olivine-phyric shergottite DAG 476 has been reported with similar pyrrhotite composition, yet this clearly results from terrestrial weathering (Lorand et al. 2005). A terrestrial origin is very unlikely for Tissint, which is an observed fall in a desert area and was collected only weeks after its fall, and is totally devoid of sulfide alteration products (i.e., Fe-oxyhydroxides). We may surmise that massive input of regolith-derived sulfur raised the fugacity of sulfur (sulfate?) to levels at which metal-deficient pyrrhotite became stable (as documented in nakhlites that bear isotopic evidence of atmospheric sulfur recycling; Chevrier et al. 2011). Then shock remelted both sulfates and sulfides, promoting additional sulfide melt exsolution concomitant with localized sulfur loss, as indicated by the progressive shift of a few pyrrhotite compositions toward the FeS-type pyrrhotite endmember in melt pockets. If pervasive devolatilization

Table 2. Selected analyses of chromite, Cr-Ti spinel, ulvöspinel, ilmenite, and magnetite in Tissint.

SiO_2	0.14	0.24	0.10	0.11	0.08	0.01	0.05	0.07	0.11	nd	0.00
Cr_2O_3	59.29	57.58	52.61	19.68	11.08	6.17	1.49	1.28	1.28	1.21	0.27
TiO_2	0.67	0.83	3.04	20.54	25.19	28.21	33.80	28.23	24.87	3.97[a]	52.92
FeO	25.78	31.47	34.30	51.95	57.64	57.44	58.31	62.35	68.01	81.55[b]	44.42
MgO	5.77	2.44	1.73	1.13	0.80	1.23	1.06	0.93	0.88	0.19	1.72
Al_2O_3	7.46	7.07	5.96	3.76	2.46	2.69	1.71	1.91	1.80	2.00	0.00
V_2O_3	0.50	0.39	0.55	0.44	0.47	0.38	0.41	0.29	0.36	nd	0.34
MnO	0.78	0.69	0.74	0.82	0.74	0.62	0.68	0.68	0.60	nd	0.73
Total	100.42	100.73	99.06	98.43	98.51	96.75	97.50	95.83	97.91	88.91	100.40
Si	0.005	0.008	0.004	0.004	0.003	0.000	0.003	0.003	0.004		0.000
Cr	1.606	1.596	1.497	0.571	0.324	0.183	0.049	0.039	0.038	0.04	0.005
Ti	0.017	0.022	0.082	0.567	0.700	0.796	0.876	0.806	0.693	0.12	0.987
Fe^{3+}	0.035	0.041	0.063	0.111	0.148	0.094	0.100	0.249	0.478	1.63	–
Fe^{2+}	0.704	0.881	0.969	1.484	1.634	1.708	1.799	1.732	1.630	1.11	0.922
Mg	0.295	0.127	0.093	0.062	0.044	0.069	0.058	0.052	0.048	0.01	0.064
Al	0.301	0.292	0.253	0.163	0.107	0.119	0.080	0.086	0.079	0.09	0.000
Mn	0.023	0.020	0.023	0.025	0.023	0.020	0.022	0.022	0.019		0.015
V	0.014	0.011	0.016	0.013	0.014	0.011	0.013	0.009	0.011		0.010

Oxide name	Chromite	Chromite	Chromite	Ti-Cr spinel	Ti-Cr spinel	Ti-Cr spinel	Ulvöspinel	Ulvöspinel	Ulvöspinel	Magnetite	Ilmenite
Spinel	15.24	14.81	12.78	8.22	5.41	5.99	4.05	4.31	3.97	4.73	
Chromite	81.27	80.89	75.71	28.86	16.36	9.20	2.46	1.94	1.89	1.92	
Ulvöspinel	1.74	2.22	8.32	57.31	70.73	80.08	88.42	81.20	69.98	11.95[a]	
Magnetite	1.75	2.08	3.19	5.61	7.49	4.73	5.07	12.54	24.15	81.40[b]	

Oxides are in wt%. Cation formulae are computed based on ideal structures of 3 cations per 4 oxygens for spinel, and 2 cations per 3 oxygens for ilmenite.

[a]Maximum value.

[b]Minimum value, assuming residual overlap.

had occurred, then Tissint would be almost S-free and metal-rich, which is not observed. Crustal sulfur assimilation and solution into shock melts explain the sulfides that decorate melted areas. This external sulfur addition is probably responsible for the metal deficiency in Tissint pyrrhotite. The fact that Ni/Fe ratios correlate with host mineral compositions (Ni-rich pyrrhotite inside olivine) indicates that the high-temperature partitioning of Fe and Ni between sulfides and silicates survived the shock event.

Oxides

The main oxide phase in Tissint is chromite, which shows zoning to intermediate Ti-Cr spinel. Ulvöspinel and ilmenite are also present as separate grains, with rare micron-sized magnetite grains close to some ulvöspinels. Oxide compositions determined by EMP are shown in Table 2 and Fig. 3. The ulvöspinels plot close to the ulvöspinel apex of the spinel prism and the ulvöspinel end of the ulvöspinel-magnetite join, and there is an almost complete series of intermediate compositions between chromite and ulvöspinel. These spinels are similar in composition to those of composite spinels in other olivine-phyric shergottites, such as EETA79001A and NWA 1110 (McSween and Treiman 1998; Goodrich et al. 2003).

Chromite cores in the lherzolitic shergottites ALH 77005 and LEW 88516, and in the basaltic shergottite EET 79001 (McSween and Treiman 1998) have similar compositions to Tissint chromite grains. The chromite rims in the lherzolitic shergottites have compositions falling in the range of Tissint Ti-Cr spinels (McSween and Treiman 1998). Tissint ulvöspinel compositions are also like those for the basaltic shergottites EET 79001 and QUE 94201 (McSween and Treiman 1998), but they are less Fe-rich than those for Shergotty titanomagnetites (Stolper and McSween 1979).

All analyzed oxide grains show bulk compositions that correspond to paramagnetic oxides at room temperature (Table 2, Fig. 3). However, magneto-optical imaging of magnetically saturated polished sections shows that some oxide grains are ferromagnetic at room temperature. Figure 4A shows an example where ferromagnetic sulfides, ferromagnetic oxides, and nonferromagnetic oxides can be seen. The ferromagnetic oxides identified by magneto-optical imaging were further analyzed by EMP, and all have ulvöspinel bulk compositions. This bulk composition should be

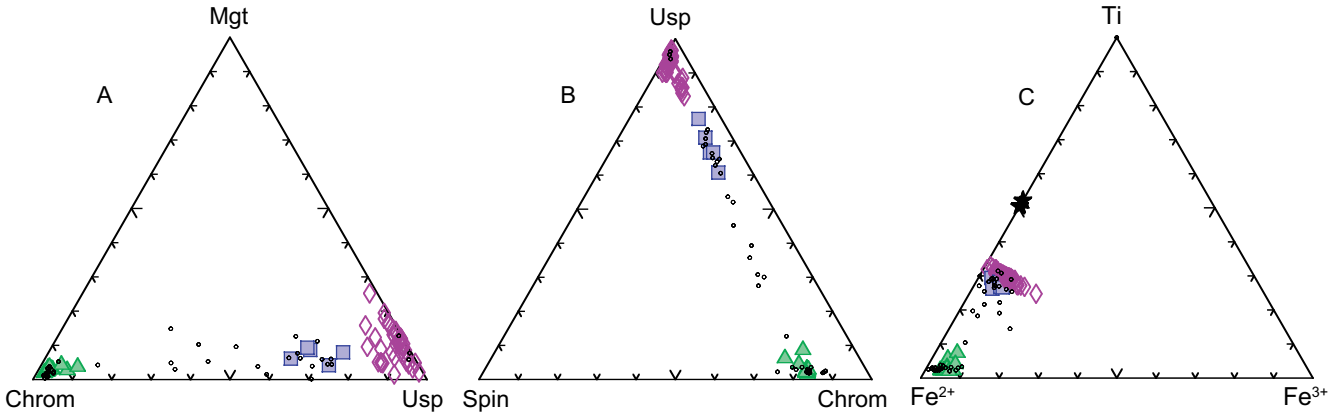

Fig. 3. Compositions of oxide minerals in Tissint. Triangles = chromite; squares = Ti-Cr spinel forming rims on chromite; diamonds = ulvöspinel; stars = ilmenite; small dots are from Chennaoui Aoudjehane et al. (2012).

paramagnetic at room temperature, so one needs to invoke the existence of ferromagnetic Fe-rich domains in the ulvöspinel. Indeed, SEM imaging shows that most ulvöspinel grains contain fine lamellae, which are somewhat deformed and displaced by shock effects (Figs. 4B and 4C). The widest lamellae (Fig. 4D) are closer to ilmenite than to ulvöspinel in probe analyses, and similar in composition to the large grains of ilmenite. The presence of ilmenite lamellae indicates oxidation-exsolution in the parent ulvöspinel along several crystallographic planes, such that the residual host spinel phase is magnetite-rich. These Fe-rich domains are too small for conventional microprobe analysis, so we pursued the problem using the SXFiveFE probe at the Cameca factory. The field emission electron column achieved a very high spatial resolution and showed that the small (mostly below 1 μm) magnetite islands seen in Figs. 4B, 4C, and 4E contain <4 wt% TiO_2. Ti-free residual spinel would require approximately 45% magnetite and approximately 55% ilmenite, roughly consistent with observed abundances (Fig. 4B).

Similar oxidation-exsolution of ulvöspinel is seen in QUE 94201 (McSween and Treiman 1998), and suggested in other shergottites (Cisowski 1986) and common in terrestrial rocks (e.g., Buddington and Lindsley 1964). While FeO in spinel is oxidized to produce magnetite, the Fe_2O_3 in a coexisting ilmenite phase may be reduced to magnetite. Righter et al. (2012) proposed a reaction in which Fe_2O_3 + FeS produce magnetite in nakhlites. The magnetite and ilmenite compositions listed in Table 2 cannot strictly be used for thermobarometry because of the residual overlap in the electron probe data. However, if we assume that the true magnetite composition lies between the value listed and pure magnetite, we calculate equilibration (Lindsley and Spencer 1982; Lepage 2003) at 300–400 °C and oxygen fugacity between FMQ-1 and FMQ-5. This is consistent with oxygen fugacities in olivine-phyric shergottites and the observation that oxidation state did not change from early- to late-stage crystallization (Goodrich et al. 2003). It suggests that the oxy-exsolution reaction occurred by cooling in a closed system without the introduction of particularly oxidizing fluids, and is not a product of the hydrothermal alteration described in Tissint by Chennaoui Aoudjehane et al. (2012).

INTRINSIC MAGNETIC PROPERTIES

The magnetic properties of Tissint are summarized in Table 3, and a list of acronyms is provided in Table S1. It is noteworthy that hysteresis properties and magnetic susceptibility, measured on bulk samples, are

Fig. 4. A) Reflected light image of a polished section of Tissint previously saturated in a field of 3 T. Two profiles cutting through sulfide and oxide grains are highlighted. The reflected light intensity (relative scale) and the vertical surface magnetic field along these profiles are indicated. Magnetic field profiles were obtained using magneto-optical imaging. The outlined sulfide is ferromagnetic, as well as oxide grains numbered 1 and 2. Oxide grain number 3 is not ferromagnetic. B) Scanning electron microscope (SEM) backscattered electron (BSE) image of a ferromagnetic oxide, with dark (ilmenite) lamellae and bright residual Fe-rich spinel host, and minor pyrrhotite on the edge of the oxide. C) SEM BSE image of a ferromagnetic oxide grain, showing faulting and deformed lamellae. The white box corresponds to the elemental map of Fig. E. D) SEM BSE image of a ferromagnetic oxide, with a wide ilmenite lamella in bright ulvöspinel host containing very fine lamellae. E) Combined elemental maps with Ti (red) and Fe (blue) Kα X-rays. Ilm, ilmenite (red), Mag, magnetite (blue), Usp, ulvöspinel (purple or violet).

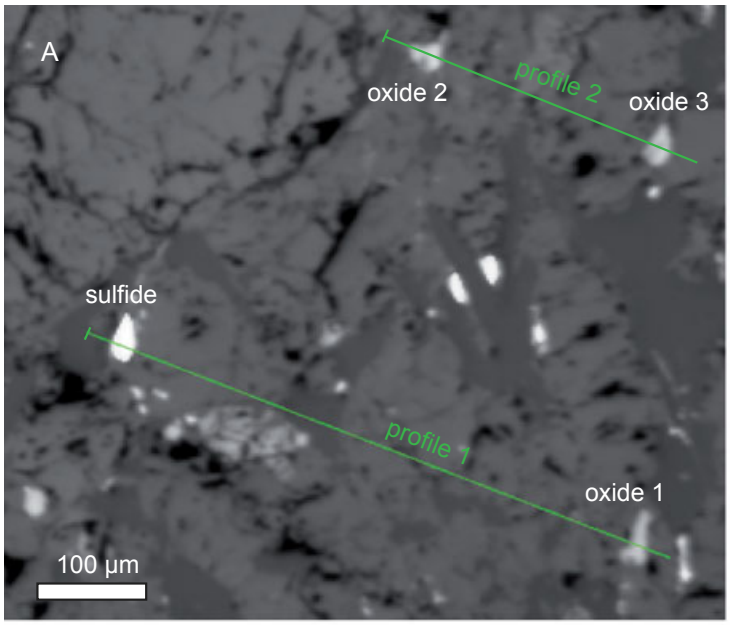
A
oxide 2
profile 2
oxide 3
sulfide
profile 1
oxide 1
100 µm

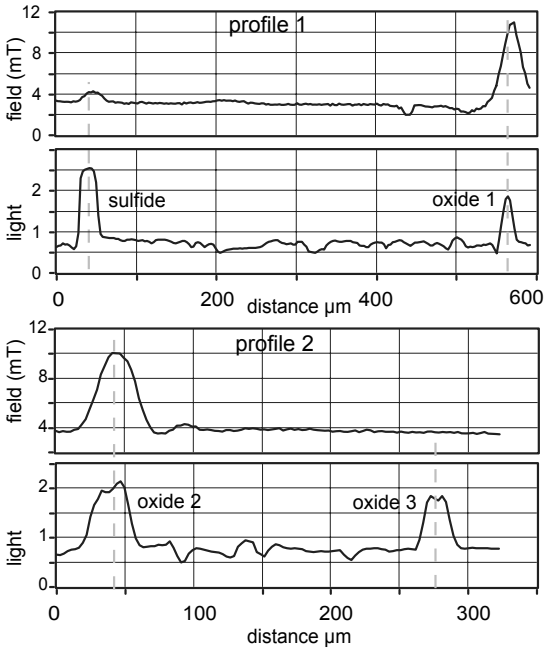
profile 1
field (mT)
light
sulfide
oxide 1
distance µm
profile 2
oxide 2
oxide 3

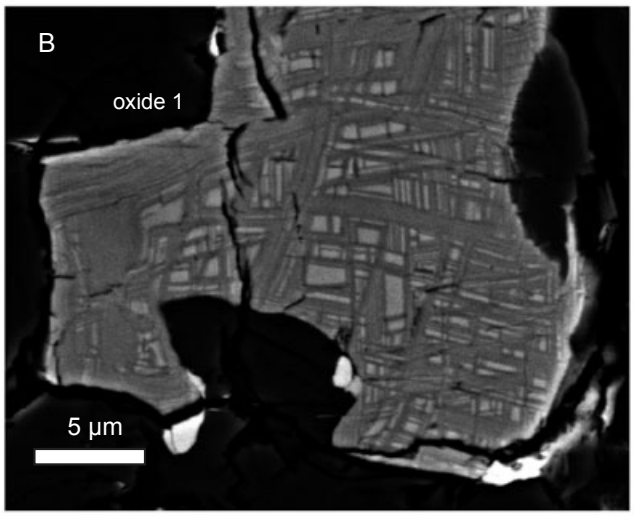
B
oxide 1
5 µm

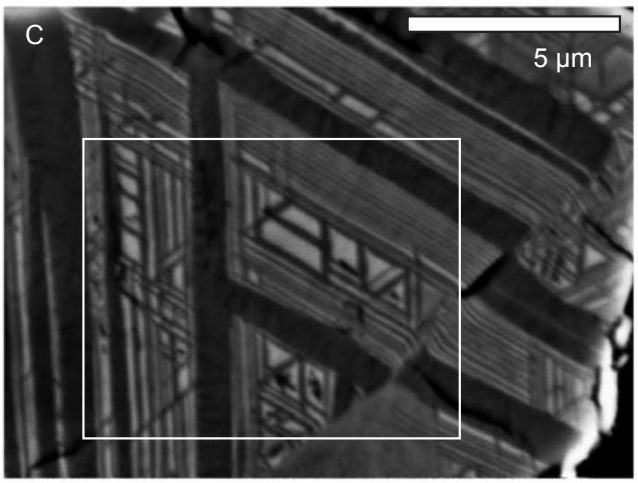
C
5 µm

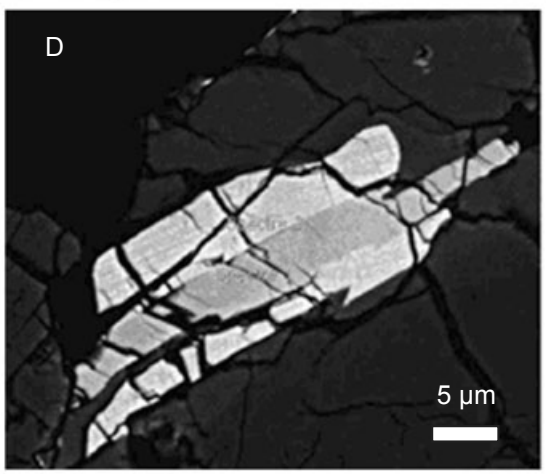
D
5 µm

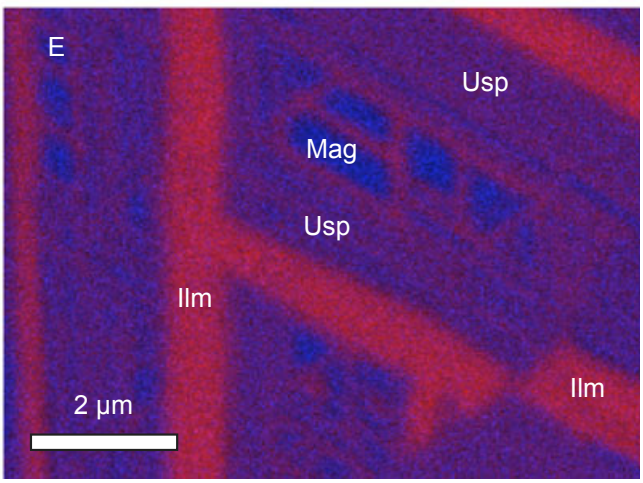
E
Usp
Mag
Usp
Ilm
Ilm
2 µm

Table 3. Magnetic properties of Tissint meteorite.

	Unit	Mean ± SD	*n*
M_{RS}	$Am^2\ kg^{-1}$	$6.23 \pm 0.82\ 10^{-2}$	16
M_S	$Am^2\ kg^{-1}$	$1.72 \pm 0.30\ 10^{-1}$	10
B_{CR}	mT	77.5 ± 4.0	10
B_C	mT	46.4 ± 2.3	10
χ	$m^3\ kg^{-1}$	$1.14 \pm 0.23\ 10^{-6}$	26
χ_f	$m^3\ kg^{-1}$	$6.86 \pm 2.05\ 10^{-7}$	26
pTRM 80 °C	$Am^2\ kg^{-1}.\mu T$	$2.18\ 10^{-7}$	1
pTRM 120 °C	$Am^2\ kg^{-1}.\mu T$	$6.45 \pm 2.45\ 10^{-7}$	3
pTRM 340 °C	$Am^2\ kg^{-1}.\mu T$	$1.29 \pm 0.06\ 10^{-5}$	3
TRM 590 °C	$Am\ kg^{-1}.\mu T$	$2.17 \pm 0.28\ 10^{-}$	3
PRM 2 GPa	$Am\ kg^{-1}.\mu T$	$2.01\ 10^{-7}$	1
PRM 1.2 GPa	$Am\ kg^{-1}.\mu T$	$1.28\ 10^{-7}$	1
PRM 0.4 GPa	$Am\ kg^{-1}.\mu T$	$5.10\ 10^{-8}$	1
NRM	$Am^2\ kg^{-1}$	$2.75 \pm 2.00\ 10^{-5}$	17

All abbreviations are defined in the text.

TRM, pTRM, and PRM intensities are normalized to the ambient field. NRM is the average for the 17 samples that were not affected by magnet contamination.

homogeneous down to the scale of at least 30 mg, i.e., approximately 10 mm^3. Therefore, in the following, all values are average values with standard deviations. The hysteresis loops (Fig. 5), the B_{CR} of 77 ± 4 mT (Table 3), the median destructive field (MDF) of SIRM of 55 mT, the S_{-300} ratio of 0.76 ± 0.02 (computed as the ratio of SIRM superimposed with a back-field IRM at 300 mT over SIRM), and the absence of saturation below 1 T (Fig. 6), all together indicate that the magnetic signal at room temperature is dominated by high-coercivity minerals. Thermal demagnetization of SIRM (Fig. 7B) shows two inflexions at about 260 °C, and in the 500–560 °C range with a maximum unblocking temperature of 585 °C. This suggests that SIRM is carried in equivalent parts by pyrrhotite (Curie temperature T_C of 290 and 320 °C for hexagonal and monoclinic forms, respectively) and a high T_C phase. Comparison of partial TRM acquired at 340 °C and total TRM (Table 3) shows that TRM is also carried in approximately equivalent parts by pyrrhotite and this high T_C phase. The hysteresis parameters B_{CR}/B_C = 1.67 ± 0.06 and M_{RS}/M_S = 0.38 ± 0.04 indicate an overall pseudosingle domain behavior. Overall, the bulk magnetic properties are in the range observed for other pyrrhotite-bearing basaltic shergottites (Rochette et al. 2005).

The determination of the high T_C phase that carries about half of SIRM and TRM is not straightforward.

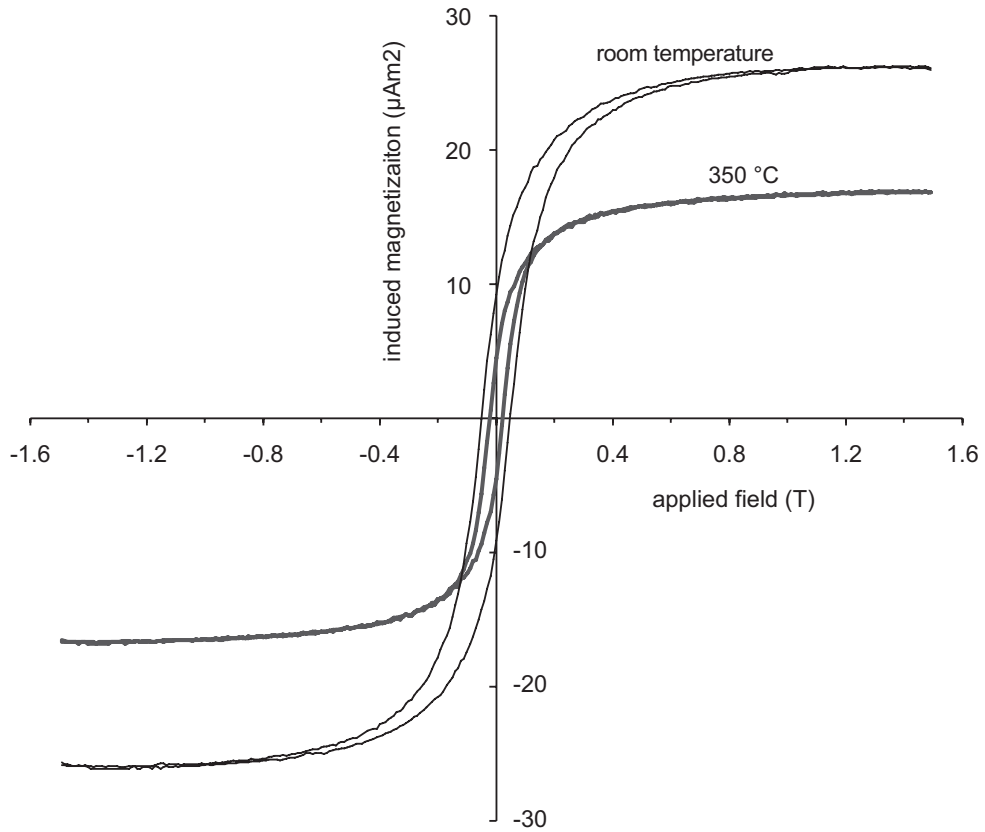

Fig. 5. Hysteresis loop at room temperature for a 140 mg sample, at room temperature and at 350 °C, after correction for high-field susceptibility computed between 1.2 and 1.5 T.

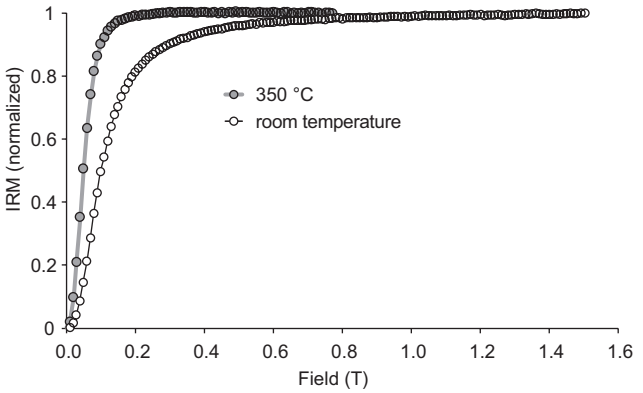

Fig. 6. Isothermal remanent magnetization versus magnetizing field at room temperature (blue circles) and at 350 °C (red circles).

This high T_C phase could be magnetite (T_C of 580 °C), a metal phase (as found in two shock-blackened Martian meteorites; Van de Moortèle et al. 2007), or a substituted hematite that has been proposed as a candidate for Martian crustal magnetism by McEnroe et al. (2002, 2004). In view of the maximum unblocking temperature of 585 °C, this titanohematite would be $Fe_{2-x}Ti_xO_3$ with $x \sim 0.1$ (Dunlop and Özdemir 1997). However, such a titanohematite should be present in large amount, at least 30 wt% based on $M_S \sim 0.5$ Am^2 kg^{-1} for titanohematite with this composition (Dunlop and Özdemir 1997) and a M_{RS}/M_S of 0.5) to account for the IRM unblocked between 350 and 600 °C. As no titanohematite has been observed by petrographic observation, this hypothesis can be clearly ruled out.

Hysteresis measurements at 350 °C, above the T_C of pyrrhotite, allow us to isolate the hysteresis properties of the high T_C phase. At this temperature, IRM saturation is reached around 250 mT (Fig. 6), and hysteresis (Fig. 5) indicates pseudosingle domain state for this high T_C phase ($B_{CR}/B_C = 1.76$, $M_{RS}/M_S = 0.26$). A high-coercivity FeNi phase, such as tetrataenite, is also excluded by the absence of significant transformation of the hysteresis properties after heating up to 650 °C in Ar or He atmosphere. Indeed, tetrataenite would transform into disordered taenite with much lower remanence above 500 °C (Wasilewski 1988). Thermomagnetic experiments reveal two Curie temperatures of 309 and 563 °C (Fig. 8) that correspond to pyrrhotite and Ti-poor titanomagnetite with as low as 3 mole% of ulvöspinel (TM03), respectively. The range of unblocking temperature observed in Fig. 7B suggests either a distribution in grain size, or, more likely, a range in Ti content of titanomagnetite grains, TM03 being the most Ti-poor titanomagnetite present. A maximum of about 15 mole% ulvöspinel can be estimated from the unblocking temperature spectrum in Fig. 8B (Lattard et al. 2006).

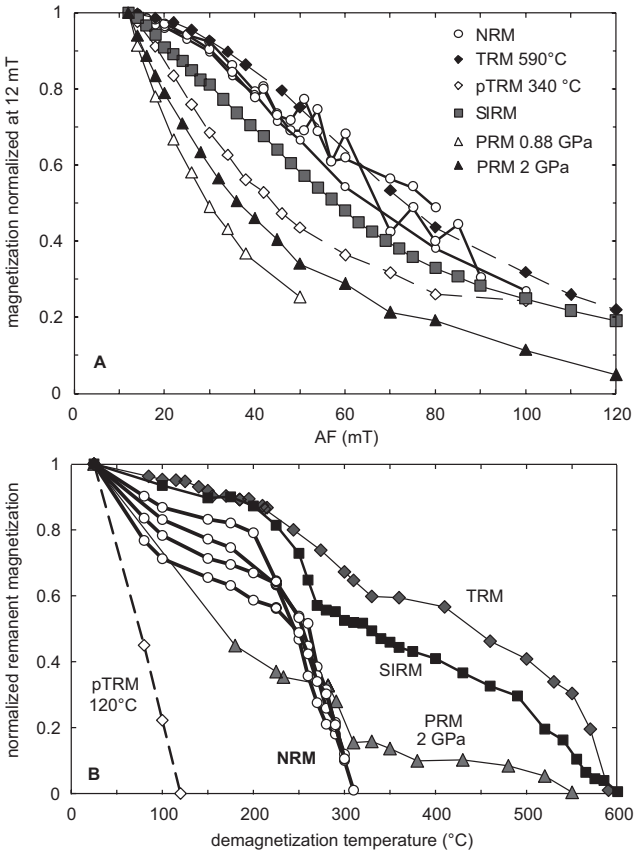

Fig. 7. AF (A) and thermal (B) demagnetization of NRM and various laboratory remanences (saturation IRM [SIRM], piezoremanent magnetization [PRM], thermoremanent magnetization [TRM], and partial thermoremanent magnetization [pTRM] at various temperatures) of Tissint. For AF demagnetization, the intensity is normalized at 12 mT to focus on the coercivity range corresponding to the stable component of the NRM. For thermal demagnetization, to take into account the two components of magnetizations (above and below approximately 150 °C), the NRM at a given temperature is the vectorial sum of the pTRM unblocked at all successive demagnetization steps.

Overall, these results point toward pseudosingle domain Ti-poor titanomagnetite for the high T_C phase, with a grain size in the 0.5–1 μm range (Dunlop 2002), in agreement with the microscopic observations discussed in the Mineralogy of Fe-Ni Sulfides section.

In view of the higher M_{RS} of magnetite with respect to pyrrhotite (by a factor 6 at most considering the same M_{RS}/M_S for both minerals, even though the room temperature M_{RS}/M_S of magnetite may be slightly lower than that of pyrrhotite), these results indicate an overall modal dominance of pyrrhotite over magnetite, by a factor 6 (mass ratio) at most. Using this ratio, $M_S = 0.17 \pm 0.03$ Am^2 kg^{-1} would correspond to the presence of approximately 0.6 wt% pyrrhotite and approximately 0.1 wt% magnetite.

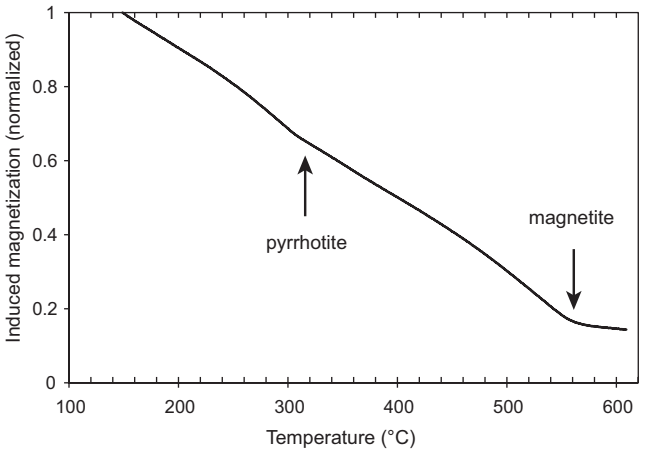

Fig. 8. Magnetization induced in a field of 300 mT as a function of temperature for a 74 mg sample of Tissint. The Curie temperatures computed from this curve using the two-tangent method (Grommé et al. 1969) are 309 and 563 °C.

Low-temperature SIRM experiments conducted after zero field cooling (ZFC) and field cooling (FC) reveal two transitions at 70 K and 120 K (Fig. 9A), in close correspondence with the Curie temperature of chromite (Klemme et al. 2000) and the Verwey transition observed for magnetite (Verwey 1939) and Ti-poor titanomagnetite composition with less than 4% Ti (Kakol et al. 1994). The M_S variation across the transition at 70 K is 0.10 $Am^2\ kg^{-1}$ (determined on a 30 mg sample), corresponding to 0.63 wt% of chromite, using a M_S of 16 $Am^2\ kg^{-1}$ for pure chromite (Robbins et al. 1971; Gattacceca et al. 2011).

The monoclinic pyrrhotite transition at 34 K is not observable in the low-temperature data (Fig. 9B). In agreement with unblocking temperatures mostly below 290 °C (Fig. 7B), this suggests that the pyrrhotite phase present in Tissint may be mostly the hexagonal form in its metastable ferromagnetic form, as typically found in other shergottites (Rochette et al. 2005). The Curie temperature of 309 °C revealed by thermomagnetic measurements (Fig. 8) is more indicative of monoclinic pyrrhotite, but this could well have formed from hexagonal pyrrhotite during the heating experiment itself. The same explanation accounts for the higher pyrrhotite unblocking temperatures for the laboratory TRM than for nonheating laboratory remanences like IRM and PRM (Fig. 7B). The ^{57}Fe Mössbauer spectra at room temperature (Fig. S2) exhibit three Fe^{2+} quadrupole doublets, associated with olivine and pyroxene (Stevens et al. 1998) superposed on weaker magnetic sextets. Two of the magnetic sextets correspond to titanomagnetite, while the four remaining magnetic sextets are consistent with pyrrhotite (Kondoro 1999). The derived hyperfine parameters are

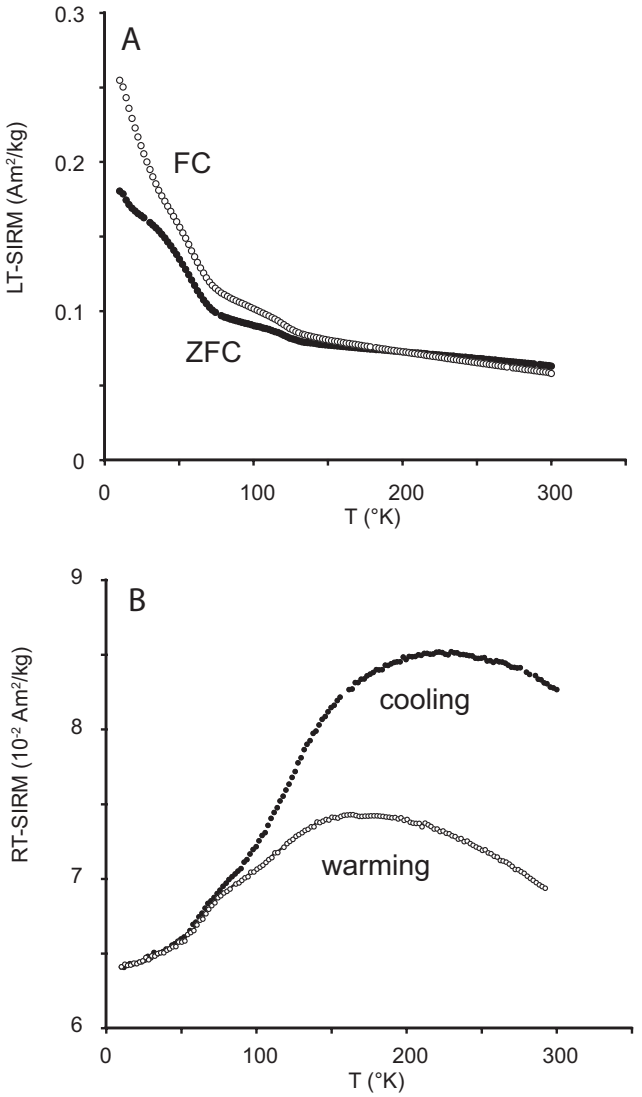

Fig. 9. Thermal evolution of A) Low-temperature saturation IRM (SIRM), B) Room-temperature SIRM.

listed in Table 4. They allow quantification of the proportion of total iron present in titanomagnetite and pyrrhotite, respectively, 2 and 4 wt%, although with very large uncertainties. Based on a total FeO content of 21 wt% (Chennaoui Aoudjehane et al. 2012), this translates into 0.5 and 0.9 wt% for pure magnetite equivalent and pyrrhotite, respectively. This is broadly consistent with other magnetic properties and petrologic investigations. Note that the signal of iron within paramagnetic oxides (chromite, ilmenite, ulvöspinel) is masked in the paramagnetic silicate doublets.

Mass-weighted average low-field magnetic susceptibility $\chi = 1.14 \times 10^{-6}\ m^3\ kg^{-1}$ is in the range observed for other pyrrhotite-bearing basaltic shergottites (mean $0.94 \pm 0.35 \times 10^{-6}\ m^3\ kg^{-1}$, $n = 12$). High-field magnetic susceptibility is $\chi_{HF} = 4.56 \pm$

Table 4. Mössbauer hyperfine parameters for Tissint meteorite. The isomer shifts are reported relative to α-Fe.

	IS (mm s^{-1})	QS (mm s^{-1})	Bhf (T)	FWHM (mm s^{-1})	A (%)	
D1	1.15	2.92	—	0.28	40.0	Olivine
D2	1.16	2.24	—	0.44	29.0	Pyroxene
D3	1.13	1.92	—	0.36	25.0	
S1	0.79	0.0	47.0	0.44	1.0	Titanomagnetite
S2	1.03	0.0	43.5	0.55	1.0	
S3	0.64	0.0	28.2	0.45	1.0	Hexagonal pyrrhotite
S4	0.69	0.0	25.0	0.45	1.0	
S5	0.60	0.0	23.5	0.45	1.0	
S6	0.61	0.0	21.5	0.45	1.0	

IS = isomet shift (±0.005); QS = quadrupole splitting (±0.005); FWHM = full width at half maximum (±0.02); A = relative area (±1%).

0.63×10^{-7} m^3 kg^{-1}, in close agreement with the paramagnetic susceptibility of 4.40×10^{-7} m^3 kg^{-1} that can be computed (see Gattacceca et al. 2008a) from the bulk composition of the meteorite (Chennaoui Aoudjehane et al. 2012). The anisotropy of magnetic susceptibility was measured on two large samples with masses 7.7 g and 28.5 g. The anisotropy degree is $P = 1.028$ (mass-weighted average) and Pf = 1.049 when corrected for the supposedly isotropic paramagnetic contribution (see Gattacceca et al. 2008a). The fabric is strongly oblate (mass-weighted average $T = 0.73$). Two measurements performed on smaller mutually oriented samples (with masses 1.32 and 0.35 g, and $P = 1.063$ and 1.072, respectively) give indistinguishable directions for the principal susceptibility axes. This weak, but well-defined, oblate, and directionally homogeneous fabric may be interpreted as the primary magmatic fabric (Gattacceca et al. 2008a) or a shock-induced fabric (Gattacceca et al. 2007; Nishioka et al. 2007). The anisotropy of SIRM, measured on two samples, is also weak and oblate with mass-weighted average $P_{SIRM} = 1.10$ and $T_{SIRM} = 0.72$.

PALEOMAGNETISM

Results

The NRM of 33 samples without fusion crust was measured. The intensity of NRM is bimodal, with 17 samples with intensity below 10^{-4} Am^2 kg^{-1} (median 2.2×10^{-5} Am^2 kg^{-1}) and 15 samples with intensity above 5×10^{-4} Am^2 kg^{-1} (median 6.9×10^{-3} Am^2 kg^{-1}). The corresponding median NRM/SIRM ratios are 3.5×10^{-4} and 1.1×10^{-1}. The higher NRM population has undoubtedly been contaminated by hand magnet, probably during meteorite hunting, or subsequent handling; unfortunately, a common practice among meteorite hunters. However, we were left with 17 samples (without fusion crust) that were suitable for paleomagnetic investigation of extraterrestrial signal.

Four samples were studied through thermal demagnetization up to 340 °C under argon atmosphere. After the removal of a stable component of magnetization between 25 and approximately 120 °C, the demagnetization was rather noisy, but a stable component was isolated in two samples between 150 and 300 °C (Fig. 10). In all four samples, the NRM is unblocked mostly above 200 °C, and is essentially demagnetized at 310 °C. Samples demagnetized by AF show a stable component of magnetization above approximately 14 mT and up to at least 100 mT (Fig. 10).

We interpret the stable magnetization isolated below 120 °C as a pTRM acquired in the Earth field during heating and cooling of the small meteorite fragments on the desert surface. Indeed, ground temperature in July at the fall location can reach about 80 °C, and can be enhanced inside small crusted meteorites because of the black fusion crust. Normalization of the demagnetization of the NRM and a pTRM imparted in the laboratory at 120 °C (in a field of 49 μT) show that the NRM unblocked below 120 °C can be accounted for by a pTRM acquired in an ambient field of 34 μT, in broad agreement with the field intensity at the fall location (41 μT). This low-temperature component of the NRM extends up to 120 °C, which is higher than the expected maximum temperature at the surface of the desert. This can be attributed to the nonideal behavior of the pseudosingle domain magnetic carriers or more likely thermo-viscous magnetization acquired during repeated heating and cooling cycles at about 80 °C in the Earth's field. Indeed, unblocking temperatures of 120 °C during the 1 hour laboratory heating correspond to a cumulative 1 month stay at approximately 65 °C for magnetite (Pullaiah et al. 1975) and approximately 100 °C for pyrrhotite (Dunlop et al. 2000), in the range of the expected thermal history of Tissint fragments at the desert surface during summer 2011.

The best demagnetization results were obtained on two samples that were first demagnetized at 120 °C, to

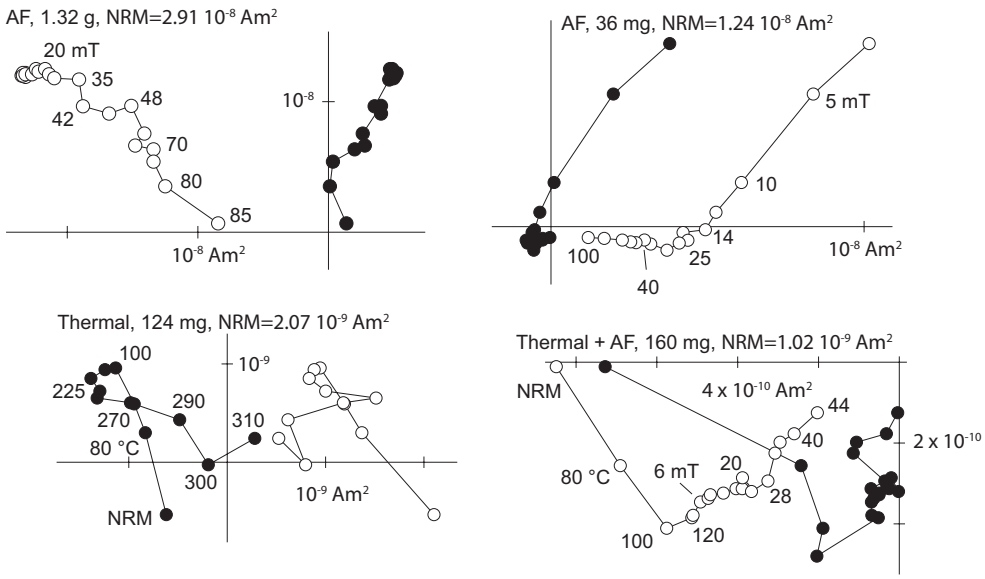

Fig. 10. Demagnetization data for four samples of Tissint. Open and solid symbols are projections on two perpendicular planes whose intersection is the horizontal axis. The axes represent magnetic moments in Am^2. The demagnetization technique, sample mass, and initial NRM moment are indicated.

remove the terrestrial pTRM, and then demagnetized by AF (Fig. 10).

There is no relation between NRM intensity and sample mass, which suggests that NRM is homogeneous in direction at least down to a scale of 30 mg (corresponding to 10 mm^3). This homogeneity is confirmed by the identical NRM direction observed in two mutually oriented samples. This high-coercivity and high-temperature magnetization cannot be a viscous remanent magnetization (because of the very short residence in the terrestrial field and the removal of a low-temperature component of magnetization) or an isothermal remanent magnetization acquired by contamination with a magnet (because of the low NRM/SIRM value), and is therefore very probably of extraterrestrial origin.

Origin of the Natural Remanent Magnetization

The comparison of the coercivity spectrum of the NRM with laboratory-induced remanences shows that the NRM is harder than all other types of remanence, except total TRM acquired at 590 °C (Fig. 7A). However, it is noteworthy that the NRM is completely unblocked at 310 °C, whereas both SIRM and laboratory TRM acquired at 590 °C have unblocking temperature extending up to 585 °C, with about half of the remanence being unblocked above 310 °C (Fig. 7B). The laboratory pTRM blocked between 590 °C and 350 °C is very hard with respect to AF (harder than total TRM), and there is no possibility that a magnetization originally blocked above 310 °C (i.e., carried by magnetite) has been erased naturally by viscous decay. Another possibility would be that the magnetite formed after cooling below approximately 310 °C. It is indeed possible that the oxidation happened in stages: the original ulvöspinel first formed ilmenite lamellae and titanium-rich titanomagnetite that was paramagnetic during cooling, and then the titanium-poor magnetite would have formed during further oxidation below approximately 310 °C. However, if formed at low temperature, magnetite should still have recorded a chemical remanent magnetization that is not observed in the NRM thermal demagnetization (e.g., Haigh 1958).

In view of the shock history of Tissint, shock remanence needs to be considered as a potential candidate. However, both the coercivity spectrum and unblocking temperature spectrum of the laboratory PRM do not fit with those of the NRM (Fig. 7). In particular, laboratory PRM at 2 GPa unblocks up to 550 °C. Even if the maximum pressure used in our experiments (2 GPa) is much lower than the peak pressure suffered by Tissint, there is no reason why a natural PRM at higher pressure would not have unblocking temperatures above 310 °C. Therefore, the most plausible explanation is that the NRM is a pTRM acquired by cooling from about 310 °C in a steady magnetic field.

However, we are left with the issue that the coercivity spectrum of the stable NRM is significantly harder than that of a pTRM acquired at 310 °C

(Fig. 7B). We attribute the fact that the NRM is harder than a pTRM at 310 °C to a combination of partial natural relaxation of the NRM with time and shocks that affected this rock after it was magnetized. Indeed, shock remagnetizes preferentially the low-coercivity fraction of the ferromagnetic minerals (e.g., Gattacceca et al. 2010b). This is confirmed by our PRM acquisition experiments up to 2 GPa: the coercivity spectrum of PRM is significantly shifted toward low AF with respect to IRM and NRM (Fig. 7A). Multiple shocks, including at least the shock that led to the ejection of the meteorite from Mars about 0.7 Myr ago, would result in increasing hardening of the NRM. Indeed, repeated pressure loadings have been shown to result in increasing demagnetization (Gilder et al. 2006; Bezaeva et al. 2007).

Scaling the NRM demagnetized between 150 and 310 °C (mean 1.34×10^{-5} Am^2 kg^{-1} for the four samples thermally) with a pTRM acquired at 310 °C and demagnetized at 150 °C, provides a rough estimate of 2.3 μT for the paleointensity of the magnetizing field. For samples demagnetized by AF, NRM/SIRM derivative ratios (REM′, see Gattacceca and Rochette 2004) were also used to estimate the paleofield necessary to account for the high-coercivity magnetization. This method, calibrated for both magnetite and pyrrhotite, provides a lower limit for the paleofield because the magnetization is a pTRM and not a TRM. The REM′ integrated over the high-coercivity component is 4.99×10^{-4} (SD = 4.11×10^{-4}, $n = 11$). This indicates a lower limit of about 1.5 μT for the paleointensity, in broad agreement with the paleointensity obtained by heating experiments.

DISCUSSION

Tissint is an olivine-phyric shergottite that has been weathered by fluids at the surface of Mars (Chennaoui Aoudjehane et al. 2012). Preliminary chronological analyses suggest a ^{147}Sm-^{144}Nd crystallization age of about 600 Ma (Brennecka et al. 2013). Tissint later suffered multiple shock events to levels sufficient to form melt veins and pockets, and ubiquitous high-pressure minerals (Baziotis et al. 2013), including shock-induced diamonds (El Goresy et al. 2013). Tissint was ejected from Mars approximately 0.7 Myr ago (Chennaoui Aoudjehane et al. 2012).

The peak shock pressure in Tissint is estimated to approximately 25 GPa with localized excursion up to 40 GPa (Baziotis et al. 2013), within the peak pressure range estimated for other shergottites, is typically 25–45 GPa (e.g., Nyquist et al. 2001; Fritz et al. 2005). In view of this shock history, it is clear that whatever its age, Tissint cannot have retained a putative primary magnetization acquired at the time of crystallization. This rock was completely remagnetized following the main impact event, by going through pressure-induced magnetic phase transition of the ferromagnetic minerals. Indeed, pyrrhotite, at least in its monoclinic form, has a phase transition at 2.8–4.5 GPa (e.g., Rochette et al. 2003; Gilder et al. 2011), and magnetite has a transition at 12–16 GPa (Ding et al. 2008), much below the peak shock pressure suffered by Tissint.

Our paleomagnetic data show that Tissint was magnetized while cooling from 310 °C down to at least 150 °C in presence of a magnetic field of about 2 μT. This excludes that the meteorite has been ejected at temperature above 150 °C because it would have cooled in space in a null magnetic field. A similar line of reasoning was used to show that ALH 84001 had never been heated above 40 °C during its ejection and transfer to Earth (Weiss et al. 2000).

The best explanation to account for thermal history of Tissint as revealed by the paleomagnetic data is postshock cooling at the Martian surface. Estimates of postshock temperature increase associated with impacts for shergottites (e.g., Fritz et al. 2005) combined with a reasonable initial temperature of 210 K for the upper surface of Martian subsurface (Mellon et al. 2004) show that a 40 GPa shock will result in a postimpact equilibrium temperature of 310 °C. This peak shock value is in good agreement with that evidenced by petrologic observations (Baziotis et al. 2013; El Goresy et al. 2013).

It may be noted that, in this scenario, a shock remanent magnetization (SRM) acquired during pressure release below about 12–16 GPa, the transition pressure of magnetite (Ding et al. 2008) should still be preserved in the rock. Although it is difficult to estimate the unblocking temperatures and the expected intensity of such a SRM, it is plausible that it is not visible during the thermal demagnetization above 310 °C because the efficiency of SRM acquisition for Tissint magnetite that has rather high coercivity (as demonstrated by the hysteresis cycle at 350 °C, Fig. 5) is probably much lower than that of TRM (e.g., Gattacceca et al. 2008b).

Our paleomagnetic data also show that this main impact event was distinct from the ejection event whose associated maximum postimpact temperature is constrained to below 150 °C, corresponding to a maximum peak pressure of about 35 GPa. In view of the young crystallization age of Tissint (approximately 600 Ma) compared with the age of the shutdown of the Martian dynamo around 4 Ga (e.g., Lillis et al. 2008), the only likely source for the 2 μT stable surface field that magnetized Tissint is the remanent magnetization of the Martian crust. Indeed, such crustal fields of

several μT are commonly expected at the present-day Martian surface (e.g., Langlais et al. 2004), and their record has already been evidenced in a number of nakhlites and shergottites (Cisowski 1986; Gattacceca and Rochette 2004). It is noteworthy that Tissint, if magnetized in a Martian dynamo magnetic field of 50 μT, would carry a remanent magnetization of only approximately 3 A m^{-1}. This is way below the 10–20 A m^{-1} that is necessary over a crustal thickness of about 40 km to account for the observed magnetic anomalies at the Martian surface, which confirms that shergottite-like rocks cannot be the source of these anomalies.

CONCLUSION

The scope of this work was to provide a detailed understanding of Tissint opaque minerals, with an emphasis on ferromagnetic phases and their magnetic record. The magnetic mineralogy of Tissint consists of about 0.6 wt% of pyrrhotite, and 0.1 wt% of low-Ti titanomagnetite (with a low ulvöspinel content in the range 3–15 mole%) for those minerals that are ferromagnetic at temperatures encountered at the Martian surface. Chromite (with a Curie temperature of 70 K) is present with an abundance of approximately 0.6 wt%. Magnetite was formed by oxy-exsolution of ulvöspinel grains during deuteric alteration. Pyrrhotites are the most Fe-poor and Ni-rich ever analyzed in shergottites and nakhlites thus far. This high Ni content reflects the large amount of Ni available inside the abundant olivine crystals that host pyrrhotite. Iron deficiency may be explained by an input of regolith-derived sulfur in agreement with other evidence of Martian weathering detected in this meteorite (Chennaoui Aoudjehane et al. 2012). These pyrrhotites probably have preserved metastable Mss structure blocked at temperature above 300 °C.

Tissint was magnetized while cooling from approximately 310 °C down to at least 150 °C in the presence of a stable magnetic field of about 2 μT that was the surface field generated by the magnetized Martian crust. This 310 °C temperature is probably the equilibrium temperature that followed the major impact suffered by Tissint, and is compatible with the peak shock pressure of 40 GPa inferred from the assemblage of high-pressure minerals. The 150 °C temperature sets an upper limit of Tissint temperature during its ejection from Mars and transfer to Earth. This emphasizes the interest of paleomagnetism for assessing the ejection temperature of Martian meteorites. The relatively weak magnetization in Tissint also confirms that shergottite-like rocks cannot be the source of the observed Martian magnetic anomalies.

Acknowledgments—The research leading to these results has received funding from Agence Nationale de la Recherche (project ANR-09-BLAN-0042), CNRS (UMR 7202), and People Programme (Marie Curie Actions) of the European Union's Seventh Framework Programme (FP7/2077-2013) under REA grant agreement no. 298355. We thank François Demory (CEREGE) and Mike Jackson (IRM) for their precious help in the laboratory, and Luc Labenne from Labenne Météorites for the loan of part of the samples. Constructive reviews by L. Taylor, T. Kohout, and an anonymous reviewer are greatly acknowledged. S. Gilder also provided useful insights on a previous version of this work.

Editorial Handling—Dr. Gretchen Benedix

REFERENCES

Acuña M. H., Connerney J. E. P., Ness N. F., Lin R. P., Mitchell D., Carlson C. W., McFadden J., Anderson K. A., Reme H., Mazelle C., Vignes D., Wasilewski P., and Cloutier P. 1999. Global distribution of crustal magnetization discovered by the Mars Global Surveyor MAG/ER experiment. *Science* 284:790–793.

Baziotis I. P., Liu Y., DeCarli P. S., Melosh H. J., McSween H. Y., Bodnar R. J., and Taylor L. A. 2013. The Tissint Martian meteorite as evidence for the largest impact excavation. *Nature Communications* 4:1404, doi:10.1038/ncomms2414.

Bezaeva N. S., Rochette P., Gattacceca J., Sadykov R. A., and Trukhin V. I. 2007. Pressure demagnetization of the Martian crust: Ground truth from SNC meteorites. *Geophysical Research Letters* 34:L23202, doi:10.1029/2007GL031501.

Brand R. A. 1995. *Normos Mössbauer fitting program, user's guide*. Starnberg, Germany: Wissenschaftlich Elektronik GmbH.

Brennecka G. A., Borg L. E., Symes S. J. K., and Wadhwa M. 2013. The age of Tissint: Sm-Nd & Rb-Sr isotope systematics of a Martian meteorite (abstract #1786). 44th Lunar and Planetary Science Conference. CD-ROM.

Buddington A. F. and Lindsley D. H. 1964. Iron-titanium oxide minerals and synthetic equivalents. *Journal of Petrology* 5:310–357.

Chennaoui Aoudjehane H., Avice G., Barrat J.-A., Boudouma O., Chen G., Duke M. J. M., Franchi I. A., Gattacceca J., Grady M. M., Greenwood R. C., Herd C. D. K., Hewins R., Jambon A., Marty B., Rochette P., Smith C. L., Sautter V., Verchovsky P., Weber P., and Zanda B. 2012. Tissint Martian meteorite: A fresh look at the interior, surface and atmosphere of Mars. *Science* 338:785–788.

Chevrier V., Lorand J.-P., and Sautter V. 2011. Sulfide petrology of four nakhlites (NWA817, NWA998, Nakhla, Governador Valadares). *Meteoritics & Planetary Science* 46:769–784.

Cisowski S. M. 1986. Magnetic studies on Shergotty and other SNC meteorites. *Geochimica et Cosmochimica Acta* 50:1043–1048.

Ding Y., Haskel D., Ovchinnikov S. G., Tseng Y.-C., Orlov Y. S., Lang J. C., and Mao H. 2008. Novel pressure-induced magnetic transition in magnetite (Fe_3O_4). *Physical Review Letters* 100:045508.

Dunlop D. J. 2002. Theory and application of the day plot (Mrs/Ms versus Hcr/Hc) 1. Theoretical curves and tests using titanomagnetite data. *Journal of Geophysical Research* 107:B3, doi:10.1029/2001JB000486.

Dunlop D. and Özdemir O. 1997. *Rock magnetism: Fundamentals and frontiers*. Cambridge, UK: Cambridge University Press. 573 p.

Dunlop D. J., Özdemir Ö., Clark D. A., and Schmidt P. W. 2000. Time-temperature relations for the remagnetization of pyrrhotite (Fe7S8) and their use in estimating paleotemperatures. *Earth and Planetary Science Letters* 176:107–116.

El Goresy A., Gillet P., Miyahara M., Ohtani E., Ozawa S., Lin Y., Feng L., and Escerig S. 2013. Multiple shock events and diamond formation on Mars (abstract #1037). 44th Lunar and Planetary Science Conference. CD-ROM.

Etaschmann B., Pring A., Putnis A., Grugic B. A., and Studer A. 2004. A kinetic study of the exsolution of pentlandite (Ni, Fe)9S8 from the monosulfide solid solution (Fe, Ni)S. *American Mineralogist* 89:39–50.

Fleet M. E. 2006. Phase equilibria at high temperatures. In *Sulfide mineralogy and geochemistry*, edited by Vaughan D. J. Reviews in Mineralogy and Geochemistry, vol. 61. pp. 365–419.

Fritz J., Artemieva N., and Greshake A. 2005. Ejection of Martian meteorites. *Meteoritics & Planetary Science* 40:1393–1411.

Gattacceca J. and Rochette P. 2004. Toward a robust normalized magnetic paleointensity method applied to meteorites. *Earth and Planetary Science Letters* 227:377–393.

Gattacceca J., Lamali A., Rochette P., Boustie M., and Berthe L. 2007. The effects of explosive-driven shocks on the natural remanent magnetization and the magnetic properties of rocks. *Physics of the Earth and Planetary Interiors* 162:85–98.

Gattacceca J., Rochette P., Gounelle M., and van Ginneken M. 2008a. Magnetic anisotropy of HED and Martian meteorites and implications for the crust of Vesta and Mars. *Earth and Planetary Science Letters* 270:280–289.

Gattacceca J., Berthe L., Boustie M., Vadeboin F., Rochette P., and De Resseguier T. 2008b. On the efficiency of shock magnetization processes. *Physics of the Earth and Planetary Interiors* 166:1–10.

Gattacceca J., Boustie M., Hood L., Cuq-Lelandais J.-P., Fuller M., Bezaeva N., de Resseguier T., and Berthe L. 2010a. Can the lunar crust be magnetized by shock: Experimental groundtruth. *Earth and Planetary Science Letters* 299:42–53.

Gattacceca J., Boustie M., Lima E. A., Weiss B. P., de Resseguier T., and Cuq-Lelandais J.-P. 2010b. Unraveling the simultaneous shock magnetization and demagnetization of rocks. *Physics of the Earth and Planetary Interiors* 182:42–49.

Gattacceca J., Rochette P., Lagroix F., Mathé P.-E., and Zanda B. 2011. Low temperature magnetic transition of chromite in ordinary chondrites. *Geophysical Research Letters* 38:L10203, doi:10.1029/2011GL047173.

Gilder S. A., Le Goff M., and Chevrin J.-C. 2006. Static stress demagnetization of single and multidomain magnetite with implications to meteorite impacts. *High Pressure Research* 26:539–547.

Gilder S. A., Egli R., Hochleitner R., Roud S. C., Volk M. W. R., Le Goff M., and de Wit M. 2011. Anatomy of a pressure-induced, ferromagnetic-to-paramagnetic transition in pyrrhotite: Implications for the formation pressure of diamonds. *Journal of Geophysical Research* 116:B10101, doi:10.1029/2011JB008292.

Goodrich C. A. 2002. Olivine-phyric Martian basalts: A new type of shergottite. *Meteoritics & Planetary Science* 37:B31–34.

Goodrich C. A., Herd C. D. K., and Taylor L. A. 2003. Spinels and oxygen fugacity in olivine-phyric and lherzolitic shergottites. *Meteoritics & Planetary Science* 38:1773–1792.

Grommé C. S., Wright T. L., and Peck D. L. 1969. Magnetic properties and oxidation of iron-titanium oxide minerals in Alae and Makaopuhi lava lakes, Hawaii. *Journal of Geophysical Research* 74:277–5294.

Gross J., Treiman A. H., Filiberto J., and Herd C. D. K. 2011. Primitive olivine-phyric shergottite NWA 5789: Petrography, mineral chemistry, and cooling history imply a magma similar to Yamato-980459. *Meteoritics & Planetary Science* 46:116–133.

Haigh G. 1958. The process of magnetization by chemical change. *Philosophical Magazine* 3:267–286.

Herd C. D. K., Borg L. E., Jones J. H., and Papike J. J. 2002. Oxygen fugacity and geochemical variations in the Martian basalts: Implications for Martian basalt petrogenesis and the oxidation state of the upper mantle of Mars. *Geochimica et Cosmochimica Acta* 66:2025–2036.

Jelinek V. 1981. Characterization of the magnetic fabric of rocks. *Tectonophysics* 79:63–67.

Kakol Z., Sabol J., Stickler J., Kozlowski A., and Honig J. M. 1994. Influence of titanium doping on the magnetocrystalline anisotropy of magnetite. *Physical Review B* 49:12767–12772.

Klemme S., O'Neill H. St. C., Schnelle W., and Gmelin E. 2000. The heat capacity of $MgCr_2O_4$, $FeCr_2O_4$, and Cr_2O_3 at low temperatures and derived thermodynamic properties. *American Mineralogist* 85:1686–1693.

Kondoro J. W. A. 1999. Mössbauer study of vacancies in natural pyrrhotite. *Journal of Alloys Compounds* 289:36–41.

Langlais B., Purucker M. E., and Mandea M. 2004. The crustal magnetic field of Mars. *Journal of Geophysical Research* 109, doi:10.1029/2003JE002048.

Langlais B., Lesur V., Purucker M. E., Connerney J. E. P., and Mandea M. 2010. Crustal magnetic fields of terrestrial planets. *Space Science Reviews* 152:223–249.

Lattard D., Engelmann R., Kontny A., and Sauerzapf U. 2006. Curie temperatures of synthetic titanomagnetites in the Fe-Ti-O system: Effects of composition, crystal chemistry, and thermomagnetic methods. *Journal of Geophysical Research* 111:B12S28, doi:10.1029/2006JB 004591.

Lepage L. D. 2003. ILMAT: An Excel worksheet for ilmenite–magnetite geothermometry and geobarometry. *Computers & Geosciences* 29:673–678.

Lillis R. J., Frey H. V., Manga M., Mitchell D. L., Lin R. P., Acuña M. H., and Bougher S. W. 2008. An improved crustal magnetic field map of Mars from electron reflectometry: Highland volcano magmatic history and the end of the Martian dynamo. *Icarus* 194:575–596.

Lindsley D. H. and Spencer K. J. 1982. Fe–Ti oxide geothermometry: Reducing analyses of coexisting Ti-magnetite (Mt) and ilmenite (Ilm). *Eos Transactions* 63:471.

Lorand J.-P., Chevrier V., and Sautter V. 2005. Sulfide mineralogy and redox conditions in some shergottites. *Meteoritics & Planetary Science* 40:1257–1272.

Lorand J.-P., Barat J.-A., Chevrier V., Sautter V., and Pont S. 2012. Metal-saturated sulfide assemblages in chassignite NWA 2737; Evidence for impact-related sulfur devolatilization. *Meteoritics & Planetary Science* 47:1830–1841, doi:10.1111/maps.12015.

McEnroe S. A., Harrison R. J., Robinson P., and Langhorst F. 2002. Nanoscale hematite–ilmenite lamellae in massive ilmenite rock: An example of lamellar magnetism with implications for planetary magnetic anomalies. *Geophysical Journal International* 151:890–912.

McEnroe S. A., Brown L. L., and Robinson P. 2004. Earth analog for Martian anomalies: Remanence properties of helo-ilmenite norites in the Bjerkreim-Sokndal intrusion, Rogaland, Norway. *Journal of Applied Physics* 56:195–212.

McSween H. Y. Jr. and Treiman A. H. 1998. Martian meteorites. In *Planetary materials*, edited by Papike J. J. Reviews in Mineralogy, vol. 36. Washington, D.C.: The Mineralogical Society of America. 53 pp.

Mellon M. T., Feldman W. C., and Prettyman T. H. 2004. The presence and stability of ground ice in the southern hemisphere of Mars. *Icarus* 169:324–340.

Nishioka I., Funaki M., and Toshimori S. 2007. Shock-induced anisotropy of magnetic susceptibility: Impact experiment on basaltic andesite. *Earth, Planets and Space* 59:e45–e48.

Nyquist L. E., Bogard D. D., Shih C.Y., Greshake D., Stöffler D., and Eugster O. 2001. Ages and geologic histories of Martian meteorites. *Space Science Reviews* 96:105–164.

Pullaiah G., Irving E., Buchan K. L., and Dunlop D. J. 1975. Magnetization changes caused by burial and uplift. *Earth and Planetary Science Letters* 28:133–143.

Quesnel Y., Sotin C., Langlais B., Costin S., Mandea M., Gottschalk M., and Dyment J. 2009. Serpentinization of the Martian crust during Noachian. *Earth and Planetary Science Letters* 277:184–193.

Righter K., Keller L. P., Rahman Z., and Christoffersen R. 2012. Exsolution of iron-titanium oxides in magnetite in Miller Range (MIL 03346) nakhlite: Evidence for post crystallization reduction in the nakhlite cumulate pile (abstract #2417). 43rd Lunar and Planetary Science Conference. CD-ROM.

Robbins M., Wertheim G. K., Sherwood R. C., and Buchanan D. N. E. 1971. Magnetic properties and site distributions in the system $FeCr_2O_4$-Fe_3O_4($Fe^{2+}Cr_{2-x}Fe_x^{3+}O_4$). *Journal of Physics and Chemistry of Solids* 32:717–729.

Rochette P., Lorand J. P., Fillion G., and Sautter V. 2001. Pyrrhotite and the remanent magnetization of SNC meteorites: A changing perspective on Martian magnetism. *Earth and Planetary Science Letters* 190:1–12.

Rochette P., Fillion G., Ballou R., Brunet F., Oulladiaf B., and Hood L. 2003. High pressure magnetic transition in pyrrhotite and impact demagnetization on Mars. *Geophysical Research Letters* 30:1683, doi:10.1029/2003GL017359.

Rochette P., Gattacceca J., Chevrier V., and Lorand J. P. 2005. Matching Martian crustal magnetization and meteorite magnetic properties. *Meteoritics & Planetary Science* 40:529–540.

Stephenson A. 1993. Three-axis static alternating field demagnetization of rocks and the identification of natural remanent magnetization, gyroremanent magnetization, and anisotropy. *Journal of Geophysical Research* 98:373–381.

Stevens J. G., Khasanov A. M., Miller J. W., Pollak H., and Li Z. 1998. *mössbauer mineral handbook*. Asheville, NC: Mössbauer Effect Data Center, The University of North Carolina.

Stolper E. and McSween H. Y. Jr. 1979. Petrology and origin of shergottite meteorites. *Geochimica et Cosmochimica Acta* 43:1475–1498.

Sutton S. R., Rao M. N., and Nyquist L. E. 2008. Sulfur and iron speciation in gas-rich impact-melt glasses from basaltic shergottites determined by microxanes (abstract #1961). 39th Lunar and Planetary Science Conference. CD-ROM.

Uehara M., van der Beek C. J., Gattacceca J., Skidanov V., and Quesnel Y. 2010. Advances in magneto-optical imaging applied to rock magnetism paleomagnetism. *Geochemistry Geophysics Geosystems* 11:Q05Y09, doi:10.1029/2009GC002653.

Van de Moortèle B., Reynard B., Rochette P., Jackson M., Beck P., Gillet P., and McMillan P. F. 2007. Shock-induced metallic iron nanoparticles in olivine-rich Martian meteorites. *Earth and Planetary Science Letters* 262:37–49.

Verwey E. J. 1939. Electronic conduction of magnetite (Fe_3O_4) and its transition at low temperature. *Nature* 144:327–328.

Walton E. L. and Spray J. G. 2003. Mineralogy, microtexture and composition of shock-induced melt pockets in the Los Angeles basaltic shergottite. *Meteoritics & Planetary Science* 38:1865–1875.

Wasilewski P. 1988. Magnetic characterisation of the new magnetic mineral tetrataenite and its contrast with isochemical taenite. *Physics of the Earth and Planetary Interiors* 52:150–158.

Weiss B. P., Kirschvink J. L., Baudenbacher F. J., Vali H., Peters N. T., Macdonald F. A., and Wikswo J. P. 2000. A low temperature transfer ALH 84001 from Mars to Earth. *Science* 290:791–795.

Yu Y. and Gee J. S. 2005. Spinel in Martian meteorite SaU 008: Implications for Martian magnetism. *Earth and Planetary Science Letters* 222:287–294.

Yu Y. J., Dunlop D. J., Özdemir O., and Ueno H. 2001. Magnetic properties of Kurokami pumices from Mt. Sakurajima, Japan. *Earth and Planetary Science Letters* 192:439–446.

SUPPORTING INFORMATION

Additional supporting information may be found in the online version of this article:

Fig S1: Plot of Tissint pyrrhotite compositions in a simplified Fe-Ni-S system (phase diagram after Fleet [2006] and references therein).

Fig S2: Mössbauer spectrum of Tissint meteorite at room temperature. D1: olivine, D2 and D3: pyroxene. The insert shows the magnetic subcomponents, S1 and S2: titanomagnetite, S3-S6: hexagonal pyrrhotite.

Table S1: Rock magnetism-related acronyms and units used in this study.

Table S2: Opaque minerals discussed in this study.